Engineering Solid Mechanics 14 (2026) 329-348

Contents lists available at GrowingScience

Engineering Solid Mechanics

homepage: www.GrowingScience.com/esm

Investigation and optimization of LM26 reinforced with MWCNT using RSM and multi-objective genetic algorithm (MOGA)

Endalkachew Mosisa Gutema[a,b*]

[a]*Department of Mechanical Engineering, College of Engineering and Technology, Wollega University, Nekemte, P.O. Box 395, Ethiopia*
[b]*Department of Mechanical and Structural Engineering and Materials Science, Faculty of Science and Technology, University of Stavanger, N-4036 Stavanger, Norway*

ARTICLE INFO

Article history:
Received 12 May 2026
Accepted 7 July 2026
Available online
7 July 2026

Keywords:
LM26 Aluminium alloy
Multi-wall Carbon Nano Tube (MWCNT)
Spindle speed
Feed rate
depth of cut
RSM
MOGA

ABSTRACT

LM26 is a cast aluminum-silicon alloy that exhibits superior castability, moderate strength, and high corrosion resistance. Silicon is typically the primary alloying agent in aluminium alloy LM26. The present study investigates the development of hybrid composites and the machining of aluminium alloy LM26 reinforced with varying weight percentages (0.25%, 0.5%, and 0.75%) of multi-wall carbon nanotubes (MWCNTs), with a focus on sustainable machining. The casting was performed by stir casting at 700°C and 650 rpm. In this study, the Central Composite design is used to design the experiment, and Response Surface Methodology (RSM) is employed to develop a quadratic (polynomial) equation using Design-Expert software V13. The milling experiment was conducted on MWCNT-reinforced LM26 material using a milling machine, with spindle speed, feed rate, depth of cut, and MWCNT percentage as parameters, to measure surface roughness (Ra) and temperature (T). Microstructural characterization of the composite was performed. The performance characteristics were analyzed using ANOVA. This result shows that wt.% of MWCNT is an influential factor in minimizing Ra, while spindle speed affects Ra, and feed rate affects temperature. Based on the results, it has been concluded that adding 0.25% wt. of MWCNTs has improved machinability; however, increasing the MWCNT content increases Ra and temperature. To achieve better machining performance that meets sustainability criteria, a Multi-Objective Genetic Algorithm was employed to optimize the objectives. The MOGA was adopted to solve the optimization problem, yielding 21 non-dominated Pareto-optimal solutions. This study has identified several alternatives to help academics and industry develop environmentally friendly, sustainable machining techniques.

© 2026 Growing Science Ltd. All rights reserved.

Abbreviations

N – Spindle Speed
f – Feed rate
a_p: Depth of cut
%: Wt. percentage of MWCNT
Al – Aluminium
MWCNT - Multi-Walled Carbon Nanotubes
GFRP – Glass Fibre Reinforced Polymer
ANOVA – Analysis of Variance
CCD – Central Composite Design
RSM – Response Surface Methodology
ANN – Artificial Neural Network
GRA – Grey Rational Analysis
SiC – Silicon Carbide
TiB2 - Titanium boride
HNT – Halloysite Nanotubes
Ep – Epoxy
Gr – Graphite
Ti–6Al–4V - Titanium alloy
PSO - Particle Swarm Optimization
GWO - Grey Wolf Optimizer
MOGA - Multi-Objective Genetic Algorithm
MQL- Minimum Quantity Lubrication
FEA - Finite Element Analysis
MRR – Material Removal Rate
MO- Multi – Objective
Al2O3 – Aluminium Oxide

1. Introduction

Aluminum LM26, a heat-treated aluminum-silicon-copper casting alloy, is widely used for its excellent mechanical properties, wear resistance, and high-temperature performance, making it a preferred choice for demanding automotive components, such as cylinder heads and other castings. The milling experiment was conducted to study the milling behavior of Al 6061 reinforced with Al_2O_3 and graphite, and optimization was carried out using RSM, with cutting speed and feed significantly influencing Ra and tool wear. (Premnath et al., 2012). Similarly, the Ra and delamination damage factor were

* Corresponding author.
E-mail addresses: endalkem5@gmail.com (E. M. Gutema)

ISSN 2291-8752 (Online) - ISSN 2291-8744 (Print)
© 2026 Growing Science Ltd. All rights reserved.
doi: 10.5267/j.esm.2026.7.001

investigated in GFRP composites using the Taguchi method integrated with an ANN to optimize the process parameters, revealing that speed and feed are the most significant machining factors in milling operations. Moreover, the work did not address the underlying physical mechanisms of delamination and fiber-matrix interactions during milling (Sreenivasulu, 2013). In another study, the Taguchi method and ANOVA were applied to evaluate the influence of milling parameters on HNT/Al/Ep composites, with ANOVA identifying the most influential factors on Ra and cutting force (Pang et al., 2014). Likewise, Karabulut (2015) designed a milling experiment using the Taguchi method, while ANOVA and ANN were employed to predict Ra and cutting force in AA7039/Al_2O_3 composites. The study concluded that material structure was the primary factor affecting Ra, whereas feed had the greatest influence on cutting force. Furthermore, RSM combined with GRA was employed to optimize milling parameters for Al7075/SiC/Al_2O_3 composites. The findings emphasized that speed and SiC weight percentage were the most significant factors affecting machinability, and that the integrated optimization approach proved more efficient than single-response optimization methods. (Rajeswari & Amirthagadeswaran, 2017). In addition, genetic algorithms were also utilized for parameter optimization. Another study applied RSM and GRA to predict cutting force, Ra, and power consumption during the milling of Al7075/SiC/Al_2O_3 composites. The results demonstrated that speed was the most influential parameter, followed by feed and depth of cut. (Malghan et al., 2017).

Chibane et al. (2017) designed a milling experiment using RSM, while regression analysis and ANOVA were employed to minimize vibration, temperature, and cutting forces in carbon/epoxy/T800S/M21 composites. Similarly, milling experiments on Al356/SiC composites were designed using the Taguchi method and optimized through the PSO technique to evaluate vibration amplitudes. The study concluded that the minimum vibration amplitudes achieved were 2.5 m/s² in the axial direction and 0.0785 m/s² in the feed direction (Sridhar et al., 2019). In another investigation, aluminium composites reinforced with 5%, 7.5%, and 10% SiC were fabricated by powder metallurgy to evaluate sintered density and hardness. The experimental results were analyzed using RSM and ANN, and it was concluded that the 7.5 wt.% SiC composite exhibited the highest sintered density and hardness (Alam et al., 2020). Furthermore, an MO experimental investigation was conducted to minimize Ra and MRR while maximizing microhardness during end milling of Al7075/SiC/Gr composites using RSM and DFA. ANOVA results indicated that feed was the most influential parameter affecting Ra and MRR, whereas speed had the greatest effect on hardness (Shihab et al., 2021). Likewise, Box–Behnken design and ANOVA were applied to identify significant factors influencing the mechanical properties of the Al7075/rice husk ash/glass powder composite system. At the same time, DFA was used to optimize the parameters. The study evaluated yield strength, ultimate tensile strength, flexural strength, impact strength, compressive strength, and microhardness (Adesina et al., 2023).

In addition, end-milling experiments on GFRP composites were conducted to minimize delamination and Ra using a combination of RSM and GWO (Priya et al., 2024). Another study investigated the wear behavior of AA5086/Al_2O_3/TiB_2 composites under varying loads and sliding speeds, revealing that the applied load was the most significant parameter affecting wear characteristics. (Manikandan et al., 2024). Similarly, the delamination factor, machining force, and Ra of plain-woven glass fabric-reinforced epoxy composites during milling were analyzed using the Taguchi method and ANOVA. The findings demonstrated that feed was the most significant factor, whereas speed had the least influence; however, the study did not integrate advanced predictive modeling techniques. (Pathak et al., 2024). An experimental investigation was conducted using RSM, and the process parameters of LM26 composites were optimized using MOGA to evaluate surface finish, hardness, and porosity. The statistical analysis revealed that intensification pressure was the most significant parameter affecting the responses. (Zeelanbasha et al., 2017). Similarly, the wear and friction behavior of LM26-reinforced SiC/Ni- Gr composites with varying SiC/Ni–Gr proportions was investigated under different loads, sliding speeds, and elevated temperatures. The experimental findings demonstrated that load and temperature had the greatest influence on the performance of both pure aluminium alloys and hybrid composites (Pawar & Kharde, 2020). Furthermore, wire electrical discharge machining (WEDM) experiments were conducted on LM26/graphite/fly ash composites to evaluate cutting force, Ra, and tool wear under various machining conditions. The results indicated that incorporating graphite and fly ash improved machinability by reducing cutting forces and enhancing surface quality (Prakash et al., 2022). In another study, mechanical properties such as tensile strength, hardness, and impact strength were evaluated to assess the effects of incorporating various reinforcements into LM26/SiC/TiO_2/Ni–Gr composites (Kumaravel et al., 2023). Likewise, Taguchi analysis was employed to minimize sliding wear in LM26/SiC/Ni–Gr composites with varying reinforcement proportions, and the results showed that the combination of 20% SiC and 2% Ni–Gr provided optimal wear resistance (Pawar et al., 2023). In addition, Prakash et al. (2025) applied the Taguchi technique to optimize machining parameters for LM26 reinforced with graphite and fly ash to minimize Ra, MRR, and overcut error. The analysis revealed that traverse speed was the most influential factor affecting both MRR and Ra (21). Similarly, the authors (Sridhar & Narayanan, 2009) investigated the influence of sintering temperature on the microstructure and density of Al–MWCNT composites with varying reinforcement proportions. Their study showed that the tensile yield strength and ultimate tensile strength improved by nearly 90% with the addition of 2 wt.% MWCNTs. Moreover, the effect of MWCNT reinforcement on the hardness, compressive strength, and microstructural characteristics of Al2024 composites was investigated. The results demonstrated that the addition of MWCNTs up to 2 vol.% maintained a relative density of 98%, increased hardness to 245 HV, and improved compressive strength to 810 MPa (Jafari,et al., 2012). Likewise, Choi et al. (2012) and Peng and Chang (2014) conducted microstructural and mechanical investigations on Al/MWCNT composites to optimize milling operations, thereby improving interfacial bonding and enhancing hardness, strength, and overall mechanical performance. Furthermore, MWCNT-reinforced AA7075 composites fabricated via powder metallurgy exhibited improved hardness, tensile strength, and dry sliding wear resistance with CNT additions up to 1 wt.%; however,

further increases in CNT content led to a decline in these properties (Peng & Chang, 2014). In another study, minimum quantity lubrication (MQL) assisted milling of Ti–6Al–4V alloy using Al_2O_3–MWCNTs was investigated, and the results indicated that cutting speed had the most significant influence on cutting energy, followed by feed and depth of cut. (Jamil et al., 2020);(Paul et al., 2017). Additionally, powder metallurgy was employed to fabricate AA7075 composites reinforced with varying proportions of MWCNTs using three different ball-milling strategies. The high-energy ball milling approach produced better dispersion and integration of nanotubes within the AA7075 matrix particles. (Feijoo et al., 2022). Finally, finite element analysis (FEA) performed in ANSYS validated the experimental findings, demonstrating that the hybrid nanocomposite containing 0.1 wt.% MWCNTs exhibited enhanced tensile, compressive, and flexural strengths (Uthale et al., 2024).

Unlike existing research, which focuses on basic aluminium alloys without accounting for nano-reinforced properties, which makes it possible to gain greater insight into the interaction between the machining process and the material, and also focuses only on composite development, mechanical testing, such as wear, impact, tensile, and fatigue tests, were performed on the developed composite. Based on recent studies, there is a substantial research gap on the machinability characteristics such as Ra, temperature, cutting force, tool wear, energy consumption, MRR, tool life, coolant/lubricant strategy, waste generation, or environmental/economic assessment etc., on LM26 aluminium metal matrix composites reinforced with MWCNTs, with the main focus being on striking the ideal balance between surface integrity and high hardness/wear resistance. This investigation is distinctive because it provides an analysis and optimization of end-milling of MWCNTs-reinforced LM26 aluminium alloy, a novel material for machining optimization studies.

The study develops predictive models for Ra and cutting temperature using RSM, and then statistically validates them using ANOVA and residual analysis to ensure model accuracy. To evaluate some critical responses, such as temperature and Ra, composites have been developed under controlled conditions. The CCD is a specialized tool within RSM that uses a limited number of experimental runs to design, analyze, and improve processes by studying the influence of various elements and their interactions. ANOVA is a statistical technique employed to test the significance, precision, and reliability of the regression equation (Elumalai & Naveen, 2026). Furthermore, MOGA integrated with the RSM models to obtain Pareto-optimal machining conditions that simultaneously minimize the competing objectives of surface quality and thermal responsiveness. The study makes a further contribution by linking machining parameters to the physical behavior of MWCNT-reinforced LM26, specifically, heat dissipation, chip formation, and the evolution of surface integrity. The integrated experimental-statistical-evolutionary framework provides a comprehensive and validated method to enhance the machining performance of advanced metal-matrix nanocomposites during end-milling operations. Researchers and industrialists can use this integrated experimental–computational strategy to develop sustainable manufacturing pathways for sophisticated aluminum nanocomposites.

2. Materials, methods, and selection of process parameters

2.1. Preparation of Materials

The LM26 aluminium ingot was purchased from M/s Jaikrishna Metals, Coimbatore, India, and the MWCNT from AdNano Technologies Pvt. Ltd, Karnataka, India. The MWCNT has a purity of 99%, a diameter of 5-20 nm, and a length of 10 μm. Table 1 shows the chemical composition of LM26. The stir casting process is used to melt Aluminium LM26 in a crucible at 700 °C with different wt.% of MWCNT (0.25%, 0.5%, and 0.75%) (Sravanthi et al., 2022; Ngoma et al., 2021; Chen et al., 2020) and are carefully stirred at a stirrer speed of 650 RPM to achieve even dispersion. After 5 minutes of mixing, the metal was formed into plates, as seen in **Fig. 1(a)**.

Table 1. Chemical composition of LM26 (Pawar et al., 2023).

LM26	Si	Mg	Fe	Cu	Mn	Aluminium (Al)
Weight %	8.4– 10.6	0.6–1.4	1.3	2.3– 4.7	≤ 0.5	Balance

Fig/ 1. Experimentation of the LM26/MWCNT specimen (a) Casted Specimen, (b) Surface Roughness Measurement, (c) Milling with temperature measurement.

2.2. Experimental Procedure

The experimental trials were carried out in a semi-automatic milling machine, as shown in **Fig. 1(b)**, under dry conditions using a carbide end mill cutter and process parameters such as N, *f,* Ap, and Wt.% were selected. According to ASTM D4417, Ra was measured using the SURFTEST SJ-201 surface roughness tester. In a Ra test, the highest peak-to-valley amplitude is obtained when testing for Ra at a perpendicular to the lay direction, which is the direction of the cutting tool machining marks. The temperature is measured using a non-contact infrared thermometer, in accordance with ASTM E2758. Without contacting the workpiece or tool, the sensor detects temperature by pointing it toward the cutting zone during milling. To ensure consistent measurement results, the thermometer's distance and orientation relative to the cutting zone were kept constant throughout the experiment. **Fig. 2** shows the experimentation flowchart.

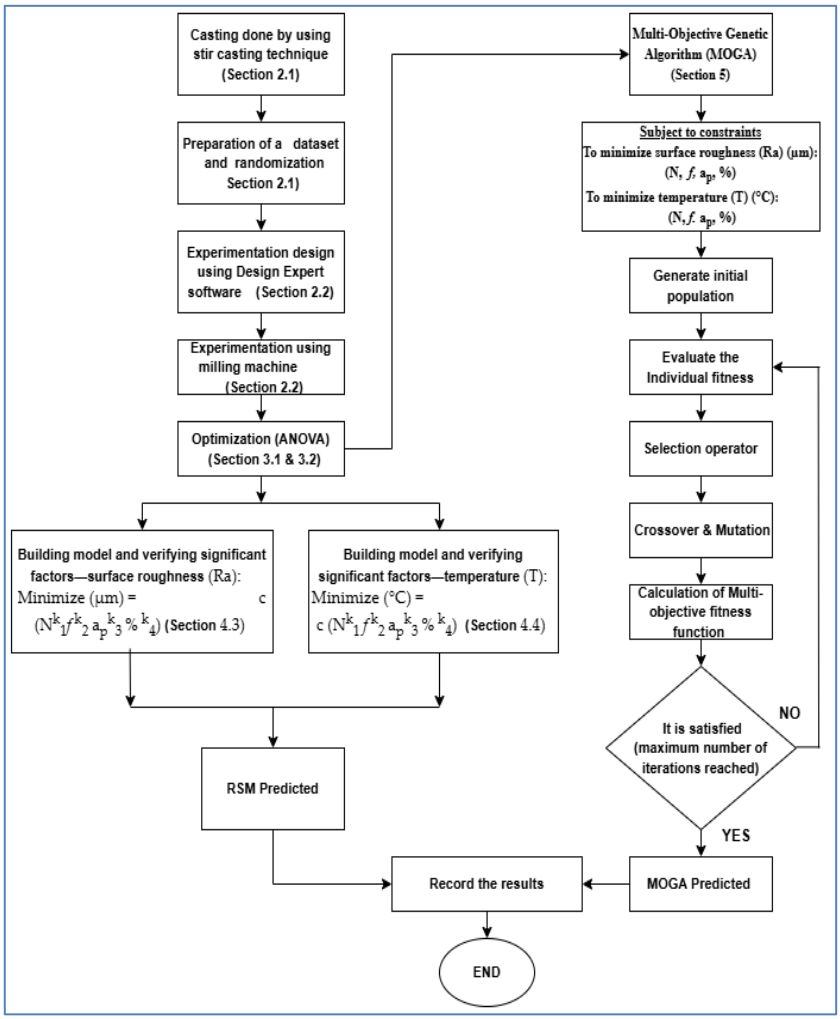

Fig. 2. Experimentation flowchart

2.3. Response Surface Methodology (RSM)

RSM was employed to develop empirical models and investigate the influence of machining parameters on Ra and temperature during end milling of MWCNT-reinforced LM26 alloy. The experiments were designed using a statistically structured design (Central Composite Design). A second-order polynomial regression model was developed to represent the relationship between input parameters and responses, expressed as:

$$Y = \beta_0 + \sum \beta_{\mathrm{i}} X_i + \sum \beta_{\mathrm{ii}} X_i^2 + \sum \beta_{\mathrm{ij}} X_i X_j + \varepsilon \quad (1)$$

where,

Y- response variable,
β_0 - constant term,
β_{i} , β_{ii} ,β_{ij} -Linear, quadratic, and interaction coefficients, respectively, and
ε - experimental error.

2.4. Process parameter identification, selection of parameter levels

For the development of empirical models and the optimization of complex engineering processes involving multiple interacting parameters, the RSM technique has been widely recognized as a statistical and mathematical tool (Calfee & Piontkowski, 2016; Gunst, 1996). In view of their significant effects on machining responses, four critical input parameters have been considered in the present investigation: N, *f*, a_p and the Wt. % as per the guidelines of Muthusamy Subramanian et al. (2017). The input parameters are selected based on the suggestions given by Pasha et al. (2022) and Sharma et al. (2024).

2.5 Development of design matrix

Each factor was varied at three levels (−1, 0, +1), and practical machining limits defined the experimental domain as shown in **Table 1**. A face-centered CCD (α = 1) was adopted because it is well-suited to constrained experimental regions. The design matrix includes 16 factorial points, 8 axial points, and 6 center points to ensure adequate curvature and estimates of experimental error. A set of 30 experiments was conducted under controlled machining conditions using the generated design matrix, and key performance responses, such as Ra and temperature, were measured as shown in **Table 3**.

$$\text{Ra: Minimize } (\mu m) = c\,(N k_1\, f k_2\, ap\, k_3\, \%\, k_4) \tag{2}$$

$$\text{T: Minimize } (°C) = \varepsilon\,(N k_1\, f k_2\, ap\, k_3\, \%\, k_4) \tag{3}$$

where K_1, k_2, k_3, k_4 and k_5 are model terms (to be estimated from experimental data), *c* is Response error for Ra and finally ε is Response error for temperature. A second-order polynomial regression model was used to relate the input variables to the responses. Because it strikes a good balance between model accuracy and computational simplicity, the second-order polynomial model has often been used in optimization studies, particularly in RSM and MOGA implementations. It can approximate complex nonlinear systems without requiring computationally demanding or excessively large experimental datasets. Analysis of variance, coefficient of determination (R^2 and adjusted R^2), and a lack-of-fit test were used to assess statistical significance at the 95% confidence level. In addition, contour and three-dimensional response surface plots were used to investigate interactions among the machining parameters. A MOGA was employed to optimize the multi-response optimization problem. After that, confirmation tests were conducted to validate the predicted optimal conditions.

Table 2. Factor and their levels

Parameter (input variables)	Units	Units Factor level		
		-1	0	+1
Spindle speed (N)	RPM	1500	2000	2500
Feed rate (*f*)	mm/rev	0.04	0.06	0.08
Depth of cut (a_p)	mm	0.5	0.6	0.7
Weight Percentage of MWCNT	%	0.25	0.5	0.75

Table 3. Design matrix and its responses

Std	Run	Factors				Response			
		N	*f*	a_p	Wt. %	Ra_{Exp}	T_{Exp}	Ra RSM_{Pred}	T °C RSM_{Pred}
24	1	2000	0.06	0.6	0.75	1.51	30.6	1.51	30.70
17	2	1500	0.06	0.6	0.5	1.50	31.8	1.48	31.99
23	3	2000	0.06	0.6	0.25	1.39	29.9	1.38	29.76
8	4	2500	0.08	0.7	0.25	1.42	31.7	1.42	31.66
30	5	2000	0.06	0.6	0.5	1.52	31.3	1.49	31.50
14	6	2500	0.04	0.7	0.75	1.53	32.3	1.53	32.22
21	7	2000	0.06	0.5	0.5	1.50	32.1	1.49	31.93
5	8	1500	0.04	0.7	0.25	1.41	30.6	1.41	30.45
29	9	2000	0.06	0.6	0.5	1.48	31.3	1.49	31.50
2	10	2500	0.04	0.5	0.25	1.36	30.3	1.36	30.24
9	11	1500	0.04	0.5	0.75	1.55	32.1	1.55	32.08
28	12	2000	0.06	0.6	0.5	1.48	31.6	1.49	31.50
16	13	2500	0.08	0.7	0.75	1.57	32.8	1.57	32.81
22	14	2000	0.06	0.7	0.5	1.51	31.9	1.51	32.03
19	15	2000	0.04	0.6	0.5	1.52	31.5	1.51	31.62
12	16	2500	0.08	0.5	0.75	1.53	31.6	1.53	31.69
15	17	1500	0.08	0.7	0.75	1.54	31.9	1.54	31.90
25	18	2000	0.06	0.6	0.5	1.47	31.7	1.49	31.50
13	19	1500	0.04	0.7	0.75	1.53	31.5	1.54	31.44
3	20	1500	0.08	0.5	0.25	1.42	31.8	1.42	31.82
11	21	1500	0.08	0.5	0.75	1.52	31.8	1.52	31.72
1	22	1500	0.04	0.5	0.25	1.42	31.3	1.43	31.36
7	23	1500	0.08	0.7	0.25	1.44	31.7	1.44	31.73
27	24	2000	0.06	0.6	0.5	1.47	31.8	1.49	31.50
6	25	2500	0.04	0.7	0.25	1.37	30.1	1.37	30.25
10	26	2500	0.04	0.5	0.75	1.51	31.9	1.51	31.93
20	27	2000	0.08	0.6	0.5	1.53	32.3	1.53	32.14
4	28	2500	0.08	0.5	0.25	1.39	30.7	1.39	30.82
18	29	2500	0.06	0.6	0.5	1.45	32.1	1.46	31.87
26	30	2000	0.06	0.6	0.5	1.47	31.2	1.49	31.50

3. Response Surface Model

3.1. Prediction of Ra (μm) using ANOVA

The experimental data are thoroughly analyzed utilizing the DESIGN EXPERT V13 program for state cases. Table 4 presents the ANOVA results to predict Ra. The table shows that the model is significant (F-value = 32.50) and that the noise level in the signal was 0.01%. The terms N, *f*, %, N*f*, N%, f^2, and %² are significant model terms, with P-values <0.0500. The Lack of Fit F-value of 0.31 indicates that the term is not significant; there is a 94.48% chance that the observed effect is due to noise, suggesting that the lack of fit is good. **Table 4** illustrates the additional adequacy measures: R^2, Adjusted R^2, and Predicted R^2. The coefficients of determination (R^2) indicate the model quality of fit; values closer to 1 indicate that the predicted R² is in reasonable agreement with the Adjusted R². The regression equation from Design Expert software, based on fundamental factors, is presented below.

$$Ra = +2.00308+0.000113\times N-12.38450\times f-1.80866\times a_p+0.836623\times \%+0.000812\times N\times f+0.000113\times N\times ap+0.000075\times N\times \%+3.43750\times f\times a_p-0.875000\times f\times \%+0.025000\times a_p\times \%--7.22807E-08\times N^2+79.82456\times f^2+1.19298\times a_p^2-0.689123\times \%^2 \quad (4)$$

In the ANOVA table, the five statistics (Standard deviation, Mean, R^2, adj R^2, and Pred R^2) are used to help explain how RSM models describe the process parameter and predict the outcome. A lower standard deviation (0.0143) indicates that the model predictions are closer to the experimental data. The predicted R^2 (0.9224) aligns reasonably with the Adjusted R² (0.9383), with a smaller difference. The quadratic model developed proved to be a good representation of the experimental data, as the lack-of-fit test indicated an insignificant p-value (p-value > 0.05).

Table 4. ANOVA table to predict Ra

Source	Sum of Squares	df	Mean Square	F-value	p-value	
Model	0.0928	14	0.0066	32.50	< 0.0001	significant
N	**0.0022**	**1**	**0.0022**	**10.90**	**0.0048**	
f	0.0014	1	0.0014	6.98	0.0185	
a_p	0.0008	1	0.0008	3.92	0.0663	
Wt. %	**0.0761**	**1**	**0.0761**	**372.99**	**< 0.0001**	
Residual	0.0031	15	0.0002			
Lack of Fit	0.0012	10	0.0001	0.3120	0.9448	not significant
Pure Error	0.0019	5	0.0004			
Cor Total	0.0958	29				
SD	0.0143			R²	0.9681	
Mean	1.48			Adjusted R²	0.9383	
				Predicted R²	0.9224	

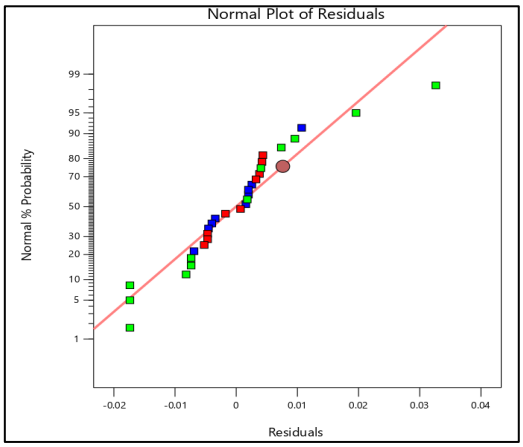

Fig. 3. Normal plot of Residuals

Fig. 3 shows the normal plot of residuals. The errors appear to be normally distributed, as they are close to a straight line.

3.1.1. Heteroscedasticity (non-constant variance) in a CCD of Ra

The lambda (λ) value is denoted by the green vertical bar in **Fig. 4**, while the confidence interval represents the permitted range of transformations. It is not necessary to transform the response values, since the selected λ value is close to 1 and lies within the confidence intervals. This means that the developed model fulfills the normality assumption and that the variances are quite homogeneous. Thus, it becomes easy to apply statistical models to the collected experimental data without any further modification. The random distribution of residuals around zero is assessed in **Fig. 5**. Residuals stand for differences between experimental and predicted values. The residual points on the chart are randomly distributed above and below the

reference line, without forming any systematic shape, such as funneling or curvature. Thus, the randomness indicates that the correlation between the process parameters and the response variable is adequately modeled by regression analysis. Moreover, the absence of any trend indicates homogeneity of variances and the impartiality and independence of errors. Therefore, the developed CCD model can be used statistically for prediction and optimization.

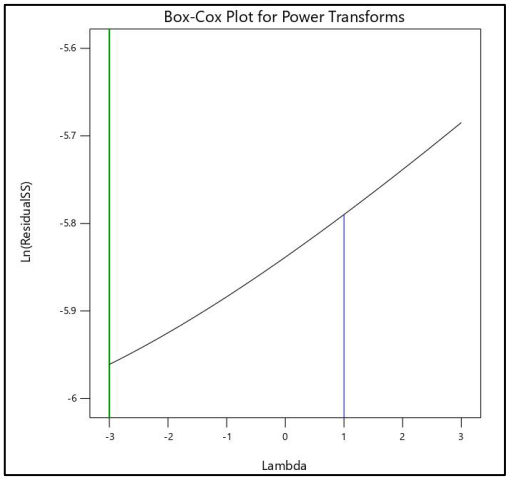

Fig. 4. Box-Cox Plot of Ra

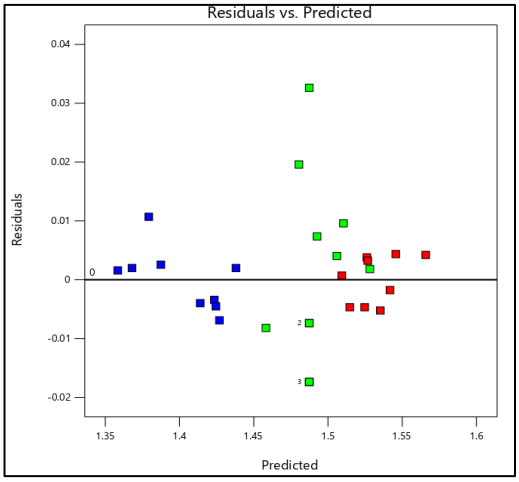

Fig. 5. Residuals vs Predicted of Ra

3.1.2. Influential-point diagnostics in a Central Composite Design (CCD) of Ra

The influential experimental runs, which have a large effect on the regression line's coefficient or intercept, are indicated on the DFBETAS chart in **Fig. 6**. The individual point illustrates the impact of a single experimental run on the regression model's intercept. The upper and lower constraint lines on the horizontal axis illustrate important influence constraints. No experimental run has had an influential impact on the regression coefficient values, since all points lie within the constraint lines. There are no outliers or significant points in the data set. The diagnostic plot DFFITS, shown in **Fig. 7**, measures the extent to which a particular observation influences the fitted response. If a particular observation is removed from the set of observations, DFFITS measures the change in the fitted response. It is evident from the above graph that the effect of any one observation on the fitted values does not dominate because all the points in the experimental runs fall within acceptable range limits. The absence of high DFFITS values indicates that the experimental data are statistically uniform.

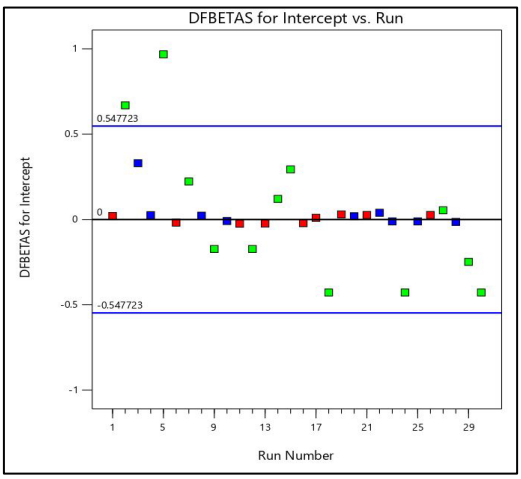

Fig. 6. DFBETAS for Intercept vs Run of Ra

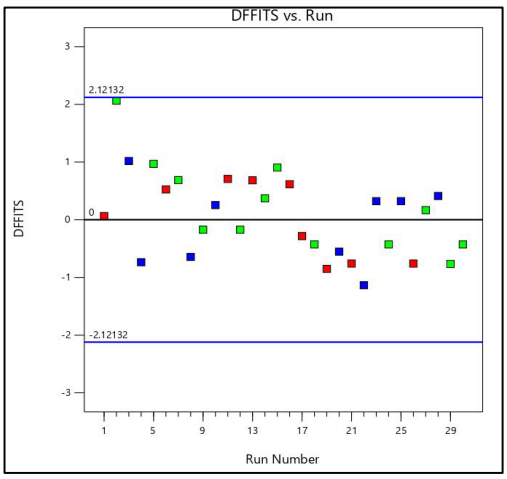

Fig. 7. DFFITS vs Run of Ra

3.1.3. Leverage analysis of Ra

The leverage value for each experimental trial in **Fig. 8** is computed based on the point's position within the design domain. As the thumb rule, experimental points with higher leverage can substantially affect the regression model. For all leverage points plotted in this figure, their leverage points remain smaller than the critical threshold marked with the reference red line. Thus, no experimental runs influence the regression relationship or control the regression modeling process. The rather evenly distributed leverage values indicate a well-balanced CCD experiment design. Taken together, these graphs (**Figs. 4-8**) demonstrate the adequacy, reliability, and absence of outlier influence on the generated CCD regression model. The analysis of DFBETAS, DFFITS, and leverage indicates that there are no outliers or runs and that the residuals are normally distributed and homoscedastic. As a result, process optimization and prediction of response parameters can be performed with confidence using the developed model.

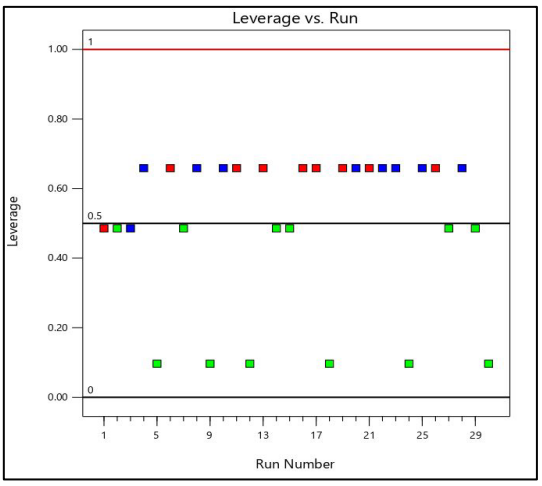

Fig. 8. Leverage analysis of Ra

3.2. Prediction of Temperature (T) using ANOVA

The first heat generation mechanism, arising from friction at the tool-workpiece contact surface; the second, arising from rubbing between the cutting edge and the workpiece surface; and the third, arising from shearing deformation in the shear zone, were introduced by the author (Feng et al., 2018). **Table 5** illustrates the ANOVA analysis used to predict temperature. The table shows that the model is significant (F = 22.69), and a noise level of 0.01% was observed in the signal. Significant model terms include f, %, Na_p, N%, $f\,a_p$, f%, N^2, f^2, a_p^2, and %², with P-values below 0.0500. The lack-of-fit F-value of 0.48 indicates that the term is not significant; however, there is 84.59% likelihood that this is due to noise, suggesting that the lack of fit is excellent. **Table 5** shows additional adequacy measures: R^2, Adjusted R^2, and Predicted R^2. The coefficients of determination (R^2) represent the models' fit and are close to 1, indicating that the Predicted R² and Adjusted R² are in reasonable agreement. The regression equation based on the actual factors is shown below.

$$\text{Temperature (T)} = +63.14459 - 0.010870\times N - 147.33918\times f - 73.47039\times a_p + 19.17061\times \% + 0.003125\times Nf + 0.004625\times Na_p + 0.001950\times N\% + 103.12500\times fa_p - 41.25000\times f\% + 2.75000\times a_p\% + 1.70526E\text{-}06\times N^2 + 940.78947\times f^2 + 47.63158\times a_p^2 - 20.37895\times \%^2 \quad (5)$$

The model's predictions are much closer to the experimental results, with a standard deviation of 0.2012. Predicted R^2 = 0.8538; adjusted R^2 = 0.9128; and R^2 = 0.9549 as shown in ANOVA table 5. For the quadratic model, the difference between the adjusted and predicted R2 values was below 0.2, indicating a respectable level of agreement. The developed quadratic model accurately describes the experimental data, with no lack of fit ($p > 0.05$).

Table 5. ANOVA table to predict Temperature (T)

Source	Sum of Squares	df	Mean Square	F-value	p-value	
Model	12.85	14	0.9180	22.69	< 0.0001	significant
N	0.0556	1	0.0556	1.37	0.2596	
f	**1.23**	**1**	**1.23**	**30.33**	< 0.0001	
a_p	0.0450	1	0.0450	1.11	0.3083	
Wt. %	**3.92**	**1**	**3.92**	**96.87**	< 0.0001	
Residual	0.6070	15	0.0405			
Lack of Fit	0.2986	10	0.0299	0.4843	0.8459	not significant
Pure Error	0.3083	5	0.0617			
Cor Total	13.46	29				
SD	0.2012		R²	0.9549		
Mean	31.51		Adjusted R²	0.9128		
			Predicted R²	0.8538		

This high degree of agreement between the experimentally obtained and predicted values may indicate that the model is overfitting. Overfitting occurs when a model not only learns the underlying relationship between the variables but also the noise present in the training set. As a result, the model performs extremely well on the current data set. Very low prediction errors may result from excessive data fine-tuning in experimental studies.

The externally studentized residuals show no outliers and are well distributed on the normal probability plot, as shown in Figure 9. All the studentized residuals lie within the control limits; therefore, the model's assumptions are satisfied.

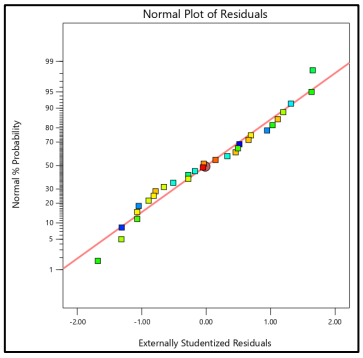

Fig. 9. Normal plot of Residuals

3.2.1. Heteroscedasticity (non-constant variance) in a CCD of Temperature.

The influence of the transformation factor λ (lambda) on the log residual sum of squares can be seen from Figure 10. The value of λ selected in the figure is close to 1 and within the confidence interval bounds, indicating that the current response data meet the necessary criteria of constant variance and normality. Therefore, there will be no need for further processing of the variable. It is evident that the selected CCD model is sufficiently statistically consistent, and the experimental data are suitable for direct regression analysis. In the present case of **Fig. 11**, no obvious systematic pattern of curvature or funnel shape can be observed. At the same time, the residuals appear to be scattered randomly around the zero reference line. The model's error terms are independent and exhibit uniform variance across the prediction range, as indicated by the observed random pattern. In addition, the absence of clustering indicates that the resulting regression model adequately captures the relationship between the response and explanatory variables.

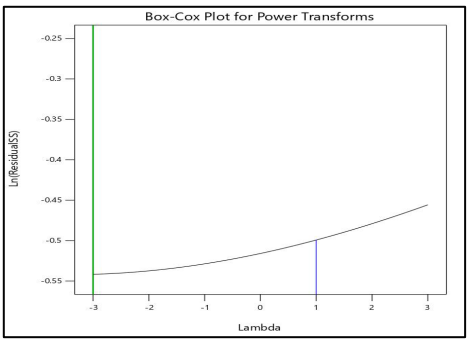

Fig. 10. Box-Cox Plot of Temperature

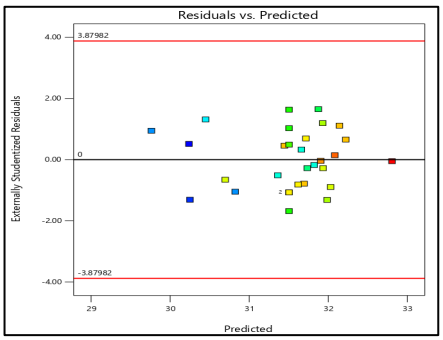

Fig. 11. Residuals vs Predicted of Temperature

3.2.2. Influential-point diagnostics in a Central Composite Design (CCD) of Temperature

Fig. 12 shows that no single experiment significantly influences the regression coefficients, since all experimental points lie within the upper and lower limits of the crucial boundary lines. The absence of extreme DFBETAS values indicates that no outliers affect our results. That is why each experiment contributes equally to constructing the regression model using the CCD method. It is evident from **Fig. 13** that none of the experimental runs has significantly influenced the estimated response values, as all points lie within the specified statistical limits. Hence, there are no critical observations. This indicates that the experimental data are statistically balanced, making the model reliable for predictions.

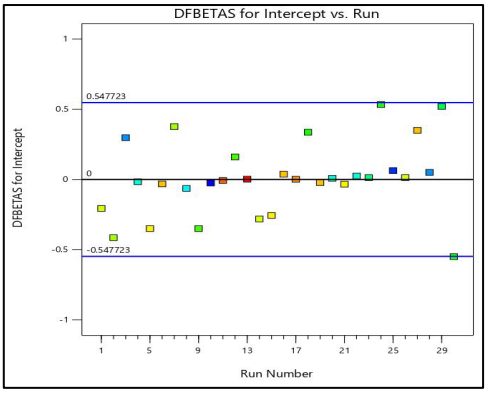

Fig. 12. DFBETAS for Intercept vs Run

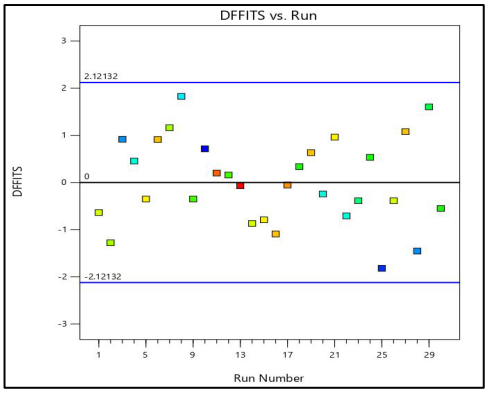

Fig. 13. DFFITS vs Run of Temperature of Temperature

3.2.3. Leverage analysis of temperature

All of the leverages in **Fig. 14** remain well below the leverage threshold, as indicated by the red horizontal line. It thus becomes clear that the regression analysis model is not dominated or influenced by any single experiment run. The CCD method for experimental design is well-balanced and appropriately designed, as evidenced by the leverage distribution. The coefficients obtained are thus statistically independent.

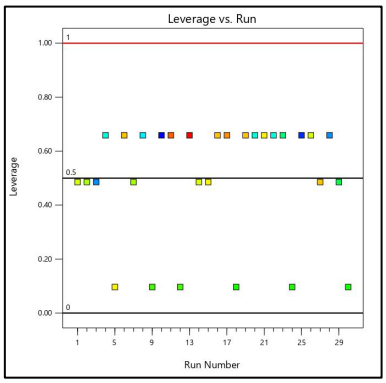

Fig. 14. Leverage analysis of Temperature

4. Results and discussion

4.1 Energy-Dispersive X-ray Analysis (EDAX) analysis

EDAX is a technique used to determine the chemical composition of materials. The microstructure of the LM26 aluminium alloy comprises pure aluminium and hybrid composites reinforced with 0.25% MWCNTs, as shown in **Fig. 15** by using a BRUKER (GERMAN) MODEL: Nano XFlash Detector with Point Scan, Area Scan, Line Scan, and Elemental Mapping.

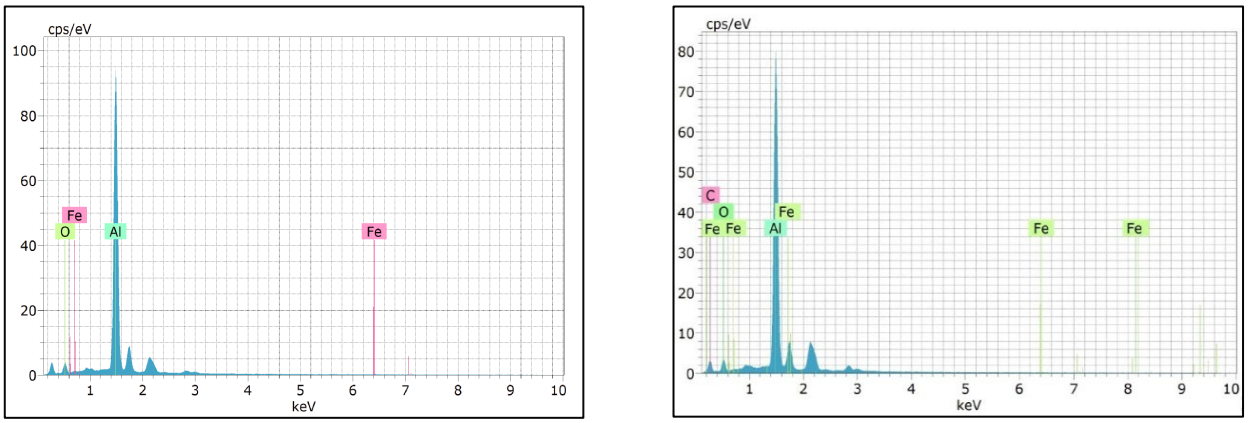

(a) (b)

Fig. 15. Energy-Dispersive X-ray Analysis (EDAX)

4.2. Microstructure analysis using SEM

A scanning electron microscope, FESEM (MAKE - CARL ZEISS (USA), MODEL - SIGMA WITH GEMINI COLUMN, RESOLUTION - 1.5 nm), has been used to study the microstructure of WMCNT-reinforced LM26 composites, as shown in Figure 3a-d. Using a precision cutter, the fabricated MWCNT-reinforced aluminum composite specimens were first cut into smaller pieces. Afterward, debris was removed from the cut specimens with acetone. The specimens were subjected to sequential grinding using SiC grit paper (220/400/600/800/1000). The specimens were polished using diamond suspension on a polishing cloth in consecutive stages. Keller's reagent (95 mL distilled water + 2.5 mL HNO_3 + 1.5 mL HCl + 1.0 mL HF) is used for etching. Beyond the general concepts of chip formation and friction, the SEM images reveal a distinct evolution in surface morphology and material reactions as the MWCNT content increases, directly affecting machining behavior.
Figure 16a shows the microstructure of the LM26 aluminium alloy. Changes in fundamental material properties markedly influence the machining response. The figure depicts the unreinforced matrix, with long, continuous grooves and severe plowing marks resulting from direct metal-to-metal contact during sliding. The lack of reinforcement causes increased plastic deformation, which increases frictional resistance, results in higher Ra, and enhances interface temperature. Furthermore, the matrix begins to exhibit smeared zones and localized adhesion, suggesting some improvement in load transfer but relatively low reinforcing capability due to agglomeration.

Fig. 16b shows the microstructure of the LM26 aluminium alloy reinforced 0.25%. In the figure, the application of MWCNTs improves the morphology of the worn surface by reducing groove depth and making the surface smoother. From the reinforcing zones, which indicate clear, dispersed reinforcement, it can be inferred that the addition of MWCNTs improved load distribution and acted as solid lubricants. This implies reduced friction and Ra due to a lower temperature generated by the rubbing process. (Dhanaraju et al., 2024) In addition, the SEM image shows a relatively uniform distribution of reinforcements at a moderate MWCNT concentration, resulting in excellent tribological performance. The absence of major delamination patches and wear debris suggests that the reinforcement successfully prevented plastic deformation of the matrix materials. **Fig. 16c** in the SEM shows that a 0.5% MWCNT composite on LM26 is strengthened in various ways, including an exceptionally high aspect ratio and efficient load transfer between the LM26 matrix and the reinforcement material (Stergioudi et al., 2022). Due to their graphitic composition, nanotubes have inherent lubricating properties and act as barriers to dislocations, thereby strengthening the matrix, limiting plastic deformation (42), and improving dispersion and cohesive adhesion between MWCNTs and the LM26 matrix. This composition exhibits relatively stable shear localization, with enhanced chip segmentation due to higher load-transfer efficiency and restricted dislocation motion. **Fig. 16d** shows the LM26/0.75%MWCNT composite becoming more apparent at this level of reinforcement. The efficient load transfer and dispersion of applied stresses in the LM26 reduce metal strain and increase the tensile and yield strengths of the composite material, which, in sliding or abrasive conditions, may experience significant increases in heat conductivity and large reductions in friction and wear rates (Biswas et al. 2023). However, clustering and pull-out tendencies are observed in the 0.75% MWCNT composition, indicating relatively poor dispersion quality and cohesive adhesion, which may lead to abrasive wear and micro-fracture during machining. Overall, the SEM analysis examined the dispersion and surface morphology of MWCNTs in the composite material. The results from the micrographs showed that there was relatively homogeneous dispersion of the MWCNTs at low content of MWCNTs, but the presence of local dense clusters of particles when the level of reinforcement is high shows the beginning of agglomeration, which arises because of the interaction of the Vander Waals forces between the nanotubes. It is also evident that there was less crack propagation and debris accumulation in some regions, showing heterogeneous stress distribution due to agglomerates of reinforcement particles. There was no indication of porosity in the micrographs; however, void-like structures may be present around agglomerates.

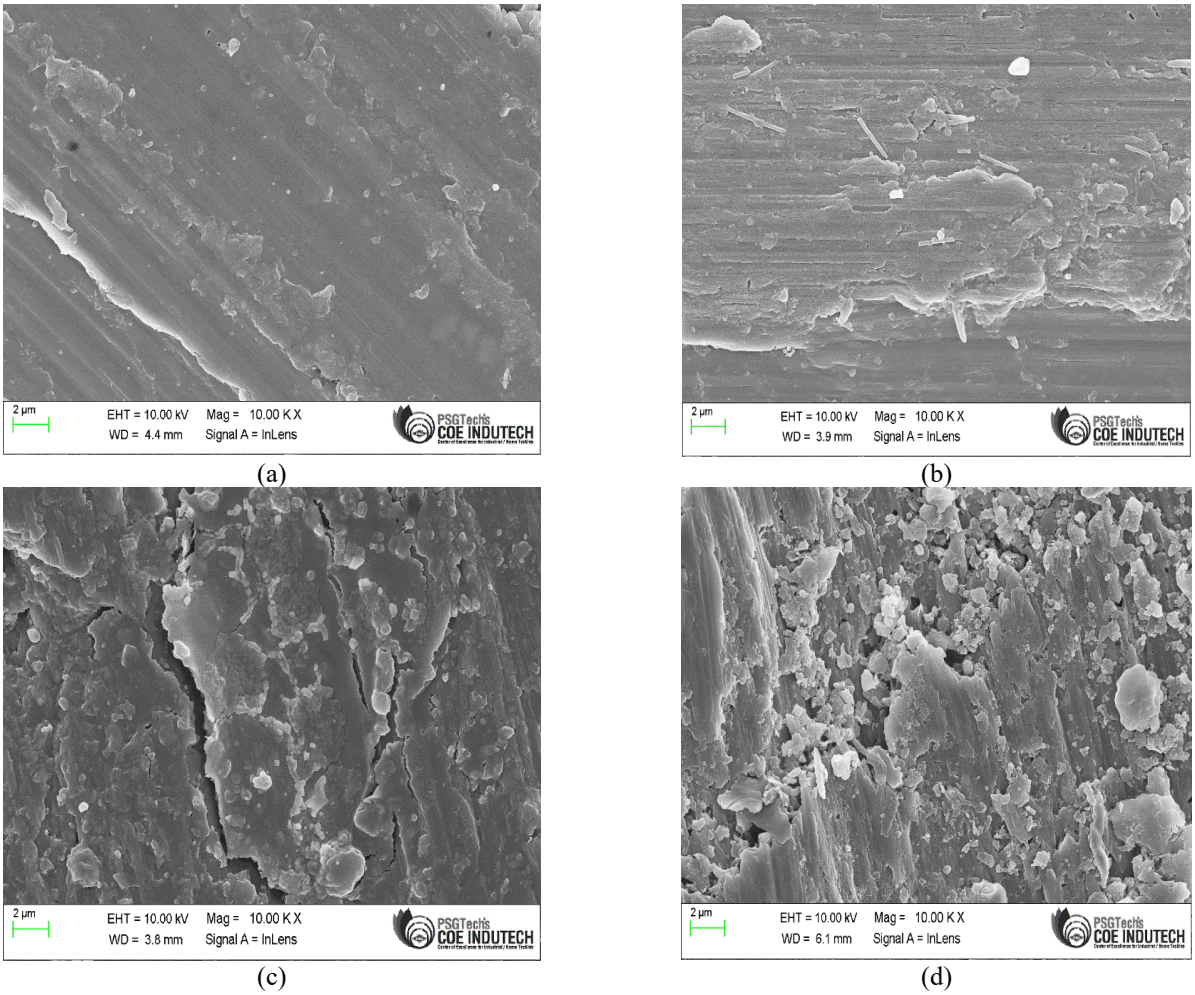

Fig. 16. Microstructure (a) Pure LM26 image Mag – 10KX; (b) 0.25% MWCNT image Mag – 10 KX; (c) 0.5% MWCNT image Mag – 10KX; (d) 0.75% MWCNT image Mag – 10KX.

4.3. Interaction effect of Ra

The 3D response surface plots in **Figs. 5(a)–(f)** illustrate how various machining parameters interact to affect the Ra of the LM26-reinforced MWCNT process, which is explored below.

Fig. 17(a) depicts the interaction plot of Ra and speed with respect to feed. The surface shows a slight slope, indicating that the roughness within the specified range is unaffected by speed or feed. Ra decreases gradually with increasing speed, indicating a minor improvement at higher speeds. As the feed increases, Ra also increases slightly. The low interaction between the two parameters is confirmed by the surface pattern, which appears smooth and far apart. The graph shows that under constant conditions, speed or feed does not affect Ra. The results show that at higher speeds, a mid-feed yields lower Ra due to interactions among chip formation, cutting forces, and machine vibration. (Kiswanto et al. 2014). **Fig. 17(b)** depicts the interaction between speed and depth of cut on Ra. Ra is minimal at 0.06 mm depth, increasing and decreasing correspondingly as depth increases and decreases, due to the appropriate dispersion and concentration of MWCNTs at that point, within the context of specified material and process characteristics. (Konsta-Gdoutos et al. 2017). It is observed that over the entire range of speed and depth of cut, the surface is nearly flat, with very little variation in Ra. **Fig. 17(c)** depicts the relationship between speed and the % concentration of MWCNT on LM26 on Ra. This curve shows a clear curvature along the MWCNT axis, indicating that Ra is largely affected by the MWCNT %. Smoother surfaces are obtained as Ra decreases, with lower MWCNT content. The gradient of the curve, as indicated by the contour map and 3D surface, confirms the dominance of the roughness by the percentage of MWCNTs (Thomas & Sreekanth 2025). The findings revealed that the industry prefers a good Ra and requires a lower MWCNT concentration. **Fig. 17(d)** depicts the interaction between feed and depth on Ra. The relatively flat surface indicates that, within this domain, feed and depth of cut do not significantly affect roughness. The changes are minimal and smooth, indicating low sensitivity to these parameters, despite a slight increase in roughness at higher feed rates. The effect on depth of cut is less significant, with contours close to horizontal suggesting a low impact. Fig. 17(e) depicts the relationship between feed and MWCNT % on Ra. The 3D surface exhibits a pronounced curvature along the MWCNT axis. This implies that the level of reinforcement significantly affects Ra, with smoother surfaces obtained at lower percentages. In addition, there is a marginal increase in Ra as feed increases. **Fig. 17(f)** depicts the interaction effects of depth and % MWCNT concentration on Ra. As the % MWCNT decreases, the surface exhibits a strong downward curvature, indicating that reinforcement content is an important factor in Ra. The moderate slope indicates a small reduction in roughness at lower depths, though the depth of cut has a negligible effect. These figures indicate that reinforcement content is the primary factor influencing Ra, compared to other parameters. The improved surface finish observed in MWCNT-reinforced LM26 may be attributed to enhanced thermal conductivity and reduced adhesion between tool and workpiece.

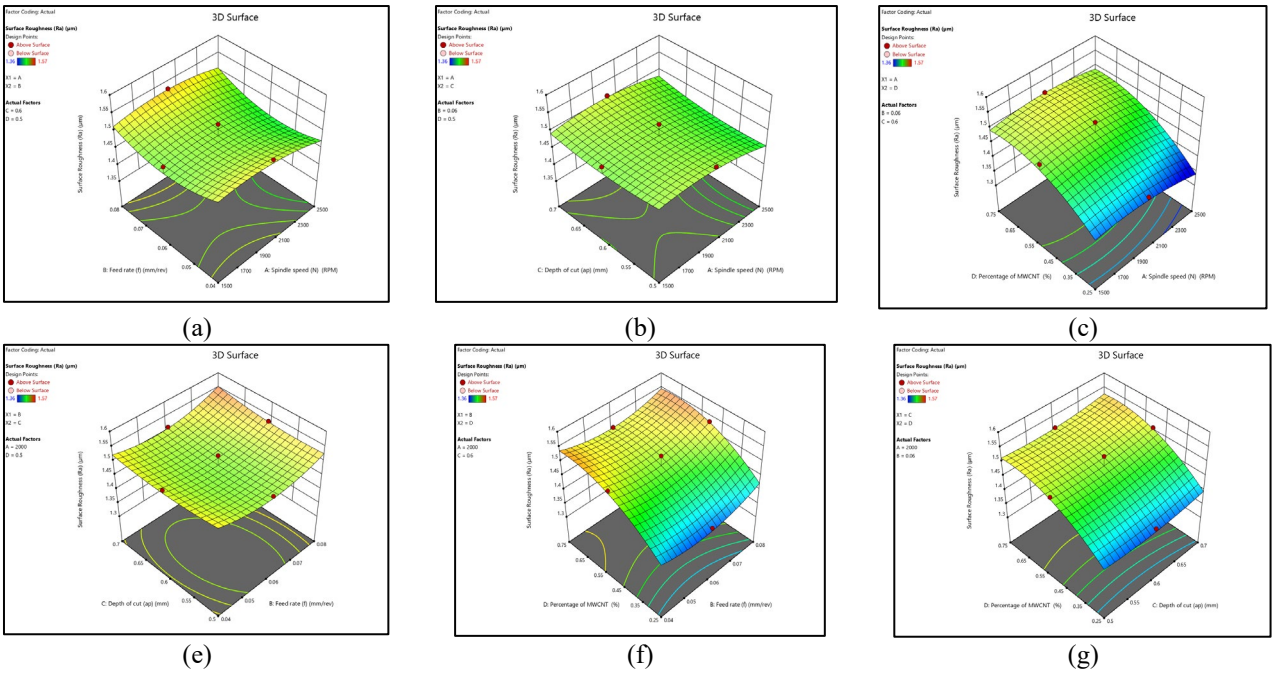

Fig. 17. Interaction effect of Ra on LM26/MWCNT

Fig. 18 compares the predicted and actual outcomes, indicating that both lie near the centerline. Influence in a regression analysis can be identified using the Cook's distance graph, as shown in **Fig. 19**. The graphical representation shows the influence of each data point on the output. The majority of Cook's distances for data points are very small, indicating little influence. None of the points is an extreme outlier, since none exceeds 1.

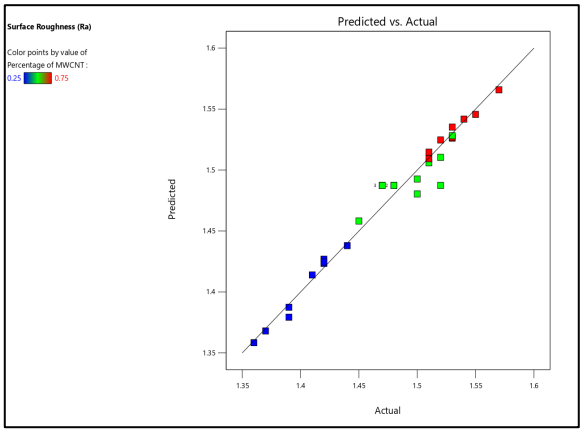

Fig. 18. Plot of predicted vs. actual.

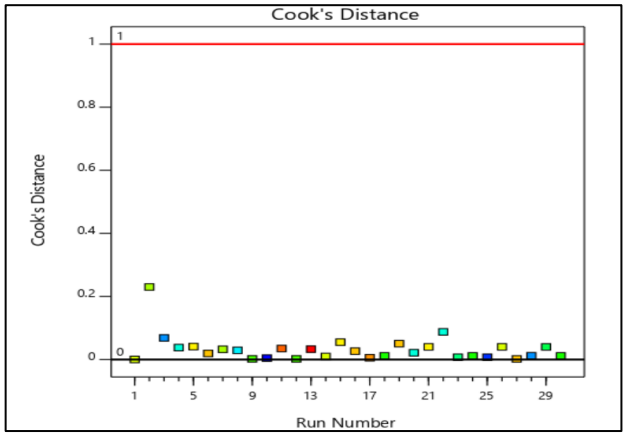

Fig. 19. Cook's distance of Ra

4.4. Interaction effect of temperature

The effect of the MWCNT-reinforced LM26 process parameter on temperature is discussed below.

Fig. 20(a) displays the interaction plot of temperature and spindle in relation to feed. This 3D surface shows the gradual increase in temperature with increasing speed or feed. Temperature is lowest at 2000 RPM and 0.06 mm/rev; thereafter, it increases in proportion to the speed and feed. The higher speed and MRR produce more frictional heat at the cutting tool's contact surface (Luo et al. 2021; Sharif., 2022), as depicted by the increasing slope of the surface along both axes. Moreover, the contour map shows the combined effect of the two parameters by displaying closely spaced curves in the top-right section of the graph. The graph above shows that temperature is directly affected by both speed and feed, as higher values produce more heat.

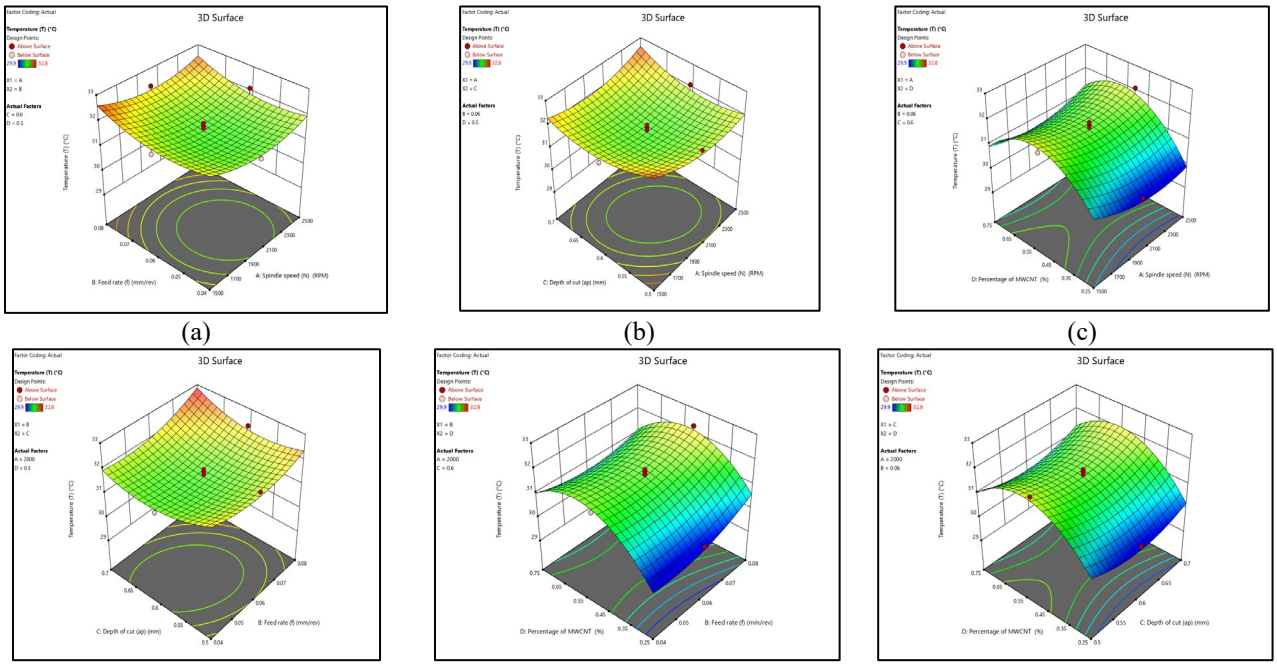

Fig. 20. Interaction effect of Ra on LM26/MWCNT

Fig. 20(b) displays the relationship between speed, depth of cut, and temperature. The figure shows a gradual, steady increase in temperature as speed and depth of cut increase. Greater depths of cut imply greater cutting pressures, whereas greater speed implies greater rubbing and shearing action, both of which contribute to greater heat output. Both variables significantly influence temperature, but speed has a greater effect than depth of cut. Thus, much higher temperatures are achieved at higher depths of cut and higher speeds.

Fig. 20(c) shows the temperature-dependent connection between speed and % of MWCNT on LM26. The surface shows a notable curvature along the reinforcement axis, indicating that the temperature is strongly affected by the MWCNT content. The temperature decreases sharply as the MWCNT percentage decreases, indicating improved conductivity and reduced

friction. (Kumanek et al. 2019). On the other hand, there is a slight increase in temperature because of the speed. The plot indicates that the % of MWCNT has a significant effect on the reduction in temperature, especially at lower speeds.
Figure 20(d) demonstrates the relationship between feed, depth, and temperature. Since the cutting force must increase to remove more material per revolution, the temperature rises with increasing feed. The effect of the depth of the cut is the same as above; i.e., when the depth of the cut is greater, the temperature increases gradually. Thus, the temperature is highly affected by the two parameters above, with the feed having a slightly greater effect.

Fig. 20(e) displays the interaction between feed and % of MWCNT at temperature. The temperature surface shows a distinct curve along the MWCNT axis, indicating that the effect of reinforcement content on heat generation is significant. The temperature decreases sharply as the MWCNT proportion decreases. The temperature increases with the feed because the cutting force and chip load generate greater heat.

The effect of reinforcement % and depth of cut on temperature is shown in **Fig. 20(f)**. The surface shows that temperature decreases with decreasing MWCNT concentration, further confirming the significance of the reinforcement factor on temperature. The effect of depth of cut is small; as cutting depth increases, temperature rises due to increased cutting force.

Fig. 21 compares predicted and actual outputs, showing that both are near the centerline. Observations that exert a substantial effect on the regression equation are identified from the plot of Cook's distance, as shown in **Fig. 22**. The higher the Cook's distance, the more influential the observation is on the regression results; each box represents one observation. This chart shows no substantial outliers, as all observations lie below the reference line marked 1. Certain observations, such as those for run numbers 8, 25, 28, and 29, are relatively high.

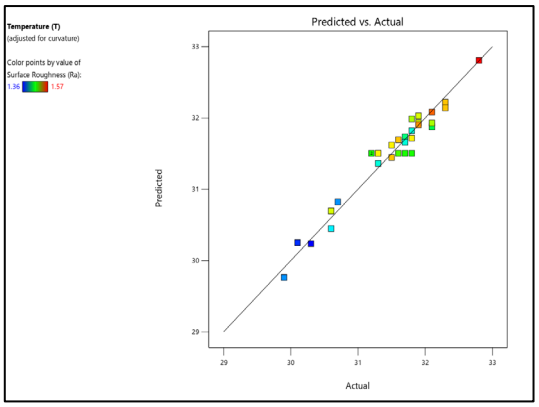

Fig. 21. Plot of predicted vs. actual.

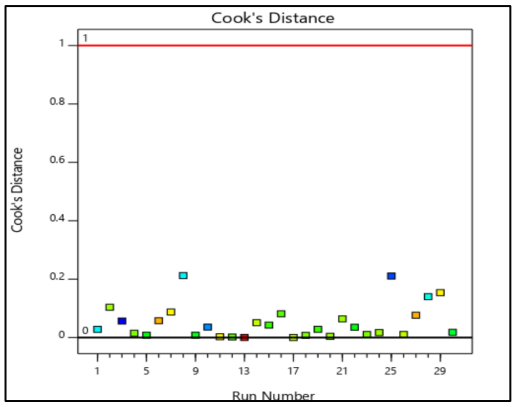

Fig. 22. Cook's Distance of Temperature.

5. Multi- Objective Optimization by using Genetic Algorithm

MOGA is an evolutionary search heuristic algorithm that employs evolutionary concepts to identify a set of optimal trade-off solutions (the Pareto front) for problems with several competing goals, rather than a single best outcome. In contrast to previous methodologies, MOGAs offer a wide range of realistic solutions that expose trade-offs (Bansal et al. 2021). A MOGA is used to predict responses. The output responses include Ra and temperature; MATLAB 2013a was used to optimize the input objective function using the MOGA method (Gopal et al. 2024; Okokpujie et al. 2021).

To minimize Ra (µm): (N, *f*, a_p, %); (6)
To minimize temperature (T) (°C): (N, *f*. a_p, %); (7)

Subject to constraints: Ra ≤ Ra limit, T≤ T

where Ra limit and T limit denote the lowest and highest limits that are essential.

5.1. Selection of parameter ranges

In selecting the ranges for its parameters, the MOGA attempts to strike a balance among preserving population diversity, searching for solutions, and converging on an optimal solution.

(i) A population of 100 was selected because it provides sufficient diversity for preservation in the search space.
(ii) The scaling function ranking: Function, stochastic uniform: Values of the fitness function are calculated using the ranking method, where the fitness of each individual is determined by its relative fitness value compared to its absolute objective value.
(iii) Mutation function: Gaussian. The method improves the algorithm's ability to perform neighborhood exploration. Since Gaussian mutation produces smooth mutations in the decision variables, it is quite efficient for continuous optimization problems.
(iv) Mutation rate: To ensure sufficient diversity in the population, the mutation rate is set to 0.1.
(v) Crossover Function: Scattered: Because it can produce highly diverse offspring through the random exchange of gene values between two parents, the dispersed crossover function is adopted.
(vi) Crossover rate: The crossover process is performed at all times when the crossover rate is 1.0. This is because it is an effective operator that can incorporate the favorable characteristics of parents.
(vii) Generations: The number of generations is fixed to 1000 to ensure that the algorithm runs for a sufficient number of cycles.

Under the parameter ranges,

$$1500 \leq N \leq 2500 \tag{8}$$
$$0.04 \leq f \leq 0.08 \tag{9}$$
$$0.5 \leq a_p \leq 0.7 \tag{10}$$
$$0.25 \leq \text{Wt. } \% \leq 0.75 \tag{11}$$

In accordance with the given constraints and operational boundaries, the first generation of possible solutions is generated at random during optimization. Selection techniques select the fittest solutions for breeding by assessing their fitness using objective functions such as minimizing Ra and temperature. The process of reproduction is followed by genetic operations, including crossover and mutation, which generate new offspring solutions, thereby maintaining diversity and preventing early convergence. The process continues for several generations until the desired number of iterations is reached. At the end of the process, the optimal solution on the Pareto frontier is selected using decision-making rules that balance the desired equilibrium among machining processes.

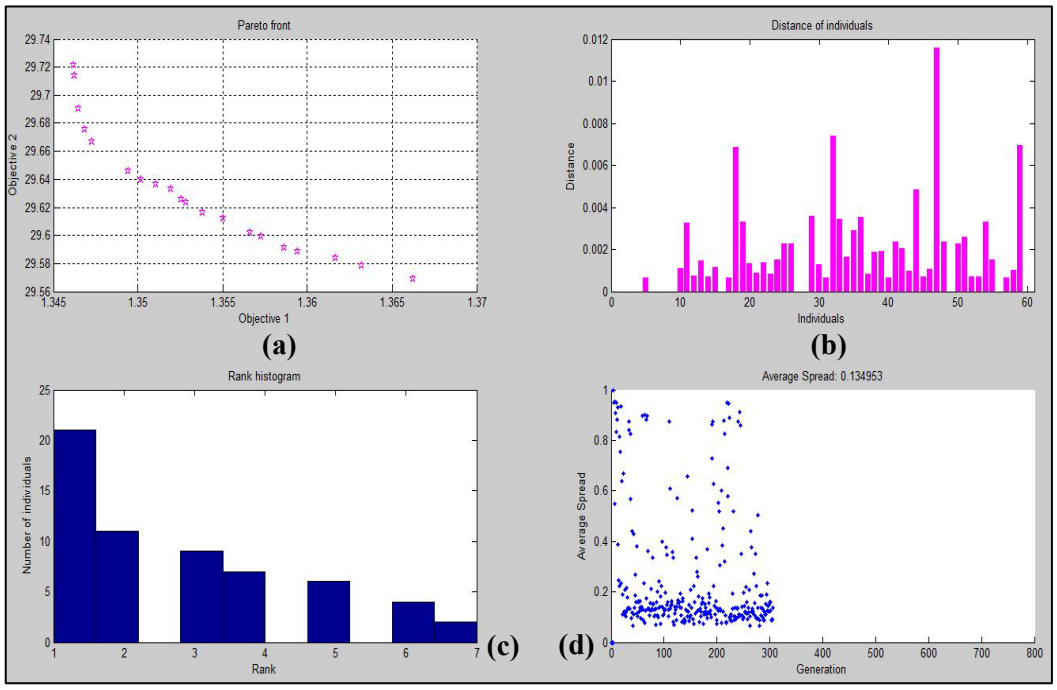

Fig. 23 depicts the performance of fitness value generation and the best and most consistent variable performances in a structured form. (a) Pareto-optimal frontier chart (b), Individual distance, (c) Individual rank histogram, and (d) Generation average spread.

5.2. Pareto-optimum solutions

Fig. 15 presents the best performances in an organized format, along with the fitness value. 23(a) Pareto-optimal frontier distribution of MOGA responses, objective 1, which refers to Ra, and objective 2, which refers to temperature. Each point on the curve represents a solution in which a decrease in one objective is matched by an increase in the other. The decreasing pattern of the Pareto-optimal frontier indicates a trade-off between the two objectives: low Ra values are associated with

slightly higher temperatures, whereas lower temperatures are associated with increased roughness. However, Pareto-optimal points tend to cluster in a small region of the design space, especially at low MWCNT content. This implies that MWCNT reinforcement stabilizes both responses, leading to only marginal changes in the optimal points. The clustering of the solutions towards the low-MWCNT region also implies that excessive inclusion of MWCNT material does not improve machining properties. Instead, process efficiency decreases due to increased thermal resistance and agglomeration. To select a Pareto solution, the decision rule can be adopted. According to the method, the optimal solution can be found near the "knee point" on the Pareto front, where a slight improvement in the first objective yields a significant loss in the other objective. Consequently, the knee point can be considered the most reasonable balance between surface quality and thermal behavior. As a result, this implies the use of average machining parameters for low- and medium-MWCNT content. Thus, Pareto optimization not only identifies mathematically optimal solutions but also helps process engineers select operating parameters to meet specific production priorities, such as quality, productivity, tool life, and thermal control. 23(b) The distance between a particular query data point and a single point in the dataset is referred to as the individual distance 23(c) The calibration and dependability of ensemble-based MOGAs can be assessed using individual rank histograms as diagnostic tools, 23(d) in optimization techniques frequently employed with MOGA, the term “generation average spread” describes the variety or dispersion of solutions (individuals) within a population across generations. Table 6 shows the clustering of input parameters for 21 sets of non-dominated Pareto-optimal solutions obtained by MOGA. The response Ra ranged from 1.34 to 1.36 µm, and the temperature ranged from 29.56 to 29.72 ^{o}C. Table 6 shows that all MOGA solutions result in excellent agreement.

Table 6. Pareto-optimum solutions

Run	Factors				Response	
	N RPM	*f* mm/rev	a_p mm	Wt. % %	Ra_{MOGA} - µm	T_{MOGA} °C
1	2407.38	0.054	0.56	0.25	1.34	**29.72**
2	2385.32	0.050	0.58	0.25	1.35	29.64
3	2256.67	0.047	0.60	0.25	**1.36**	**29.56**
4	2406.68	0.052	0.57	0.25	1.34	29.67
5	2404.40	0.051	0.57	0.25	1.34	29.66
6	2344.76	0.050	0.59	0.25	1.35	29.61
7	2407.35	0.054	0.56	0.25	1.34	29.71
8	2361.43	0.049	0.59	0.25	1.35	29.61
9	2365.33	0.049	0.58	0.25	1.35	29.62
10	2376.39	0.050	0.58	0.25	1.35	29.63
11	2406.67	0.054	0.57	0.25	1.34	29.69
12	2287.73	0.047	0.59	0.25	1.36	29.57
13	2311.11	0.048	0.59	0.25	1.35	29.58
14	2333.15	0.049	0.59	0.25	1.35	29.60
15	2366.11	0.050	0.58	0.25	1.35	29.63
16	2361.07	0.051	0.59	0.25	1.35	29.62
17	2388.29	0.051	0.58	0.25	**1.34**	29.64
18	2327.31	0.049	0.59	0.25	1.35	29.59
19	2320.45	0.048	0.59	0.25	1.35	29.59
20	2361.44	0.049	0.59	0.25	1.35	29.61
21	2294.32	0.047	0.59	0.25	1.36	29.58

6. Confirmatory test

Milling results for MWCNT-reinforced LM26 alloy are confirmed by the confirmatory test, as shown in Table 7. The error percentage is within ±2%, indicating that the analysis is reliable.

Table 7. Confirmatory test

Run	N	*f*	a_p	Wt. %	Ra $MOGA_{Pred}$	Ra $MOGA_{obs}$	Error	Temp $MOGA_{Pred}$ - (T)	Temp $MOGA_{obs}$ - (T)	Error
	RPM	mm/rev	mm	%	µm	µm	%	°C		%
2	2385.32	0.050	0.58	0.25	1.35	1.335	1.11	29.64	29.60	0.134
5	2404.40	0.051	0.57	0.25	1.34	1.349	-0.67	29.66	29.63	0.101

7. Conclusion

The experiment is conducted using a central composite design (CCD) on a milling machine with MWCNT-reinforced LM26, and the results are analyzed using Design-Expert software. The performance characteristics of Ra and temperature are analyzed using ANOVA. The interaction effects of the cutting parameter are examined. MOGA is used to optimize machining parameters. Based on the interaction effect and the surface plot, the following conclusion can be drawn.

- The ANOVA results indicate that the % of MWCNT is the most influential factor affecting Ra and temperature, followed by speed on Ra and feed on temperature.

- In relation to the interaction effect, the minimum Ra is achieved at a speed of 1900 to 2300 RPM; feed of 0.05 to 0.07 mm/rev; depth of cut of 0.6 mmm and Wt. % of MWCNT of 0.25.
- In the analysis, the minimum temperature was observed at a speed of 2100 RPM, a feed of 0.06 mm/rev, a depth of cut of 0.6 mm, and a % of MWCNT of 0.25.
- It is observed that the developed regression model for Ra has a correlation coefficient of 96.81% and a predicted R^2 of 92.24%, and for temperature, the correlation coefficient is 95.49%, and the predicted R^2 is 85.38%.
- MATLAB generated 21 non-dominated Pareto-optimal solutions using the MOGA. The response Ra ranged from 1.34 to 1.36 μm, and the temperature ranged from 29.56 to 29.72 °C.
- The confirmatory test is performed, and the percentage of error is in good agreement with the measured values.

Author Contributions: Conceptualization, EMG; methodology, EMG; software, EMG; validation, EMG; formal analysis, EMG; investigation, EMG; data curation, EMG; writing, EMG —original draft preparation, EMG and; writing, EMG — review and editing, EMG; visualization: EMG. The author has read and agreed to the published version of the manuscript.

Funding: The research was supported by the INDMET project (Grant No. 62862) funded by the NORHED II program.

Institutional Review Board Statement: Not applicable.

Informed Consent Statement: Not applicable.

Data Availability Statement: The original contributions presented in this study are included in the article. Further inquiries can be directed to the corresponding author.

Conflicts of Interest: The authors declare no conflict of interest.

References

Alam, M. A., Hamdan, H. Y., Azeem, M., Hussain, P. B., bin Salit, M. S., Khan, R., ... & Ansari, A. H. (2020). Modeling and optimization of hardness behavior of sintered Al/SiC composites using RSM and ANN: A comparative study. *Journal of Materials Research and Technology*, *9*(6), 14036-14050.

Adesina, O. S., Akinwande, A. A., Balogun, O. A., Adediran, A. A., Sanyaolu, O. O., & Romanovski, V. (2023). Statistical Analysis and Optimization of the Experimental Results on Performance of Green Aluminum-7075 Hybrid Composites. *Journal of Composites Science*, *7*(3). https://doi.org/10.3390/jcs7030115

Bansal, S., Singh, M., Dubey, R. K., & Panigrahi, B. K. (2021). Multi-objective Genetic Algorithm-Based Deep Learning Model for Automated COVID-19 Detection Using Medical Image Data. *Journal of Medical and Biological Engineering*, *41*(5), 678–689. https://doi.org/10.1007/s40846-021-00653-9

Biswas, P., Prajapati, P. K., Bapanapalle, C. O., Sadhu, K. K., Ghosh, R., & Mandal, N. (2023). Effect of MWCNTs on micromechanical and high-temperature tribological behavior of ZTA-MgO ceramic composites. *Materials Today Communications*, *35*, 105869. https://doi.org/10.1016/j.mtcomm.2023.105869

Calfee, R., & Piontkowski, D. (2016). Design and analysis of experiments. In *Handbook of Reading Research*. https://doi.org/10.2460/ajvr.1980.41.02.300

Chen, L., Hou, Z., Liu, Y., Luan, C., Zhu, L., & Li, W. (2020). High-strength and high-ductility copper matrix composite reinforced by a graded distribution of carbon nanotubes. *Composites Part A: Applied Science and Manufacturing*, *138*(August), 106063. https://doi.org/10.1016/j.compositesa.2020.106063

Chibane, H., Serra, R., & Leroy, R. (2017). Optimal milling conditions of aeronautical composite material under temperature, forces and vibration parameters. *Journal of Composite Materials*, *51*(24), 3453–3463. https://doi.org/10.1177/0021998316687626

Choi, H. J., Shin, J. H., & Bae, D. H. (2012). The effect of milling conditions on microstructures and mechanical properties of Al/MWCNT composites. *Composites Part A: Applied Science and Manufacturing*, *43*(7), 1061-1072.

Dhanaraju, G., Pittala, R. K., Ben, B. S., Atgur, V., Banapurmath, N. R., Umarfarooq, M. A., Khan, T., & Singh, B. (2024). Enhanced mechanical performance and damping behavior of CFRP composites through exfoliated MWCNT functionalization. *Nanocomposites*, *10*(1), 184–200. https://doi.org/10.1080/20550324.2024.2335698

Elumalai, B., & Naveen, P. (2026). CCD-ANOVA based RSM approach for heat transfer optimization in Cross-Hybrid (MoS2-SiO2) nanofluid flow. *Results in Engineering*, *29*, 109274. https://doi.org/10.1016/j.rineng.2026.109274

Feijoo, I., Pena, G., Cristóbal, M. J., Cabeza, M., & Rey, P. (2022). Effect of Carbon Nanotube Content and Mechanical Milling Conditions on the Manufacture of AA7075/MWCNT Composites. *Metals*, *12*(6). https://doi.org/10.3390/met12061020

Feng, Y., Pan, Z., & Liang, S. Y. Temperature prediction in Inconel 718 milling with microstructure evolution. The International Journal of Advanced Manufacturing Technology. (2018); 95(9), 4607-4621. Available from: https://doi.org/10.1007/s00170-018-1581-1

Gopal, M., Gutema, E. M., Lemu, H. G., & Sori, J. (2024). A Hybrid Nondominant-Based Genetic Algorithm (NSGA-II) for Multiobjective Optimization to Minimize Vibration Amplitude in the End Milling Process. *Advances in Materials Science*

and Engineering, *2024*. https://doi.org/10.1155/2024/6652973

Gunst, R. F. (1996). Response Surface Methodology: Process and Product Optimization Using Designed Experiments. *Technometrics*, *38*(3), 284–286. https://doi.org/10.1080/00401706.1996.10484509

Jafari, M., Abbasi, M. H., Enayati, M. H., & Karimzadeh, F. (2012). Mechanical properties of nanostructured Al2024-MWCNT composite prepared by optimized mechanical milling and hot pressing methods. *Advanced Powder Technology*, *23*(2), 205–210. https://doi.org/10.1016/j.apt.2011.02.008

Jamil, M., Khan, A. M., Hegab, H., Gupta, M. K., Mia, M., He, N., Zhao, G., Song, Q., & Liu, Z. (2020). Milling of Ti–6Al–4V under hybrid Al2O3-MWCNT nanofluids considering energy consumption, surface quality, and tool wear: a sustainable machining. *International Journal of Advanced Manufacturing Technology*, *107*(9–10), 4141–4157. https://doi.org/10.1007/s00170-020-05296-9

Kiswanto, G., Zariatin, D. L., & Ko, T. J. (2014). The effect of spindle speed, feed-rate and machining time to the surface roughness and burr formation of Aluminum Alloy 1100 in micro-milling operation. *Journal of Manufacturing Processes*, *16*(4), 435–450. https://doi.org/10.1016/j.jmapro.2014.05.003

Konsta-Gdoutos, M. S., Danoglidis, P. A., Falara, M. G., & Nitodas, S. F. (2017). Fresh and mechanical properties, and strain sensing of nanomodified cement mortars: The effects of MWCNT aspect ratio, density and functionalization. *Cement and Concrete Composites*, *82*, 137–151. https://doi.org/10.1016/j.cemconcomp.2017.05.004

Kumanek, B., & Janas, D. (2019). Thermal conductivity of carbon nanotube networks: A review. *Journal of Materials Science*, *54*(10), 7397–7427.

Kumaravel, P., Venkatesh Raja, K., & Suresh, P. (2023). Mechanical behavior of LM26/SiC/TiO2/Ni-Gr reinforced hybrid metal matrix composites – An experimental investigation. *Journal of Ceramic Processing Research*, *24*(3), 569–577. https://doi.org/10.36410/jcpr.2023.24.3.569

Luo, H., Fu, J., Wu, T., Chen, N., & Li, H. (2021). Numerical simulation and experimental study on the drilling process of 7075-t6 aerospace aluminum alloy. *Materials*, *14*(3), 1–17. https://doi.org/10.3390/ma14030553

Malghan, R. L., Rao, K. M. C., Shettigar, A. K., Rao, S. S., & D'Souza, R. J. (2017). Application of particle swarm optimization and response surface methodology for machining parameters optimization of aluminium matrix composites in milling operation. *Journal of the Brazilian Society of Mechanical Sciences and Engineering*, *39*(9), 3541–3553. https://doi.org/10.1007/s40430-016-0675-7

Manikandan, M., Prabhavathi, K., Santhosh Kumar, C., Al-Attabi, K., & Saxena, A. (2024). ANOVA Study on Wear Parameters in Aluminum metal matrix Nano Composites. *E3S Web of Conferences*, *491*, 1–10. https://doi.org/10.1051/e3sconf/202449102023.

Muthusamy Subramanian, A. V., Nachimuthu, M. D. G., & Cinnasamy, V. (2017). Assessment of cutting force and surface roughness in LM6/SiCp using response surface methodology. *Journal of applied research and technology*, *15*(3), 283-296.

Ngoma, M. M., Mathaba, M., & Moothi, K. (2021). Effect of carbon nanotube loading and pressure on the performance of a polyethersulfone (PES)/carbon nanotube (CNT) membrane. *Scientific Reports*, *11*(1), 1–13. https://doi.org/10.1038/s41598-021-03042-z

Okokpujie, I. P., Ohunakin, O. S., & Bolu, C. A. (2021). Multi-objective optimization of machining factors on surface roughness, material removal rate, and cutting force on end-milling using MWCNTs nano-lubricant. *Progress in Additive Manufacturing*, *6*(1), 155–178. https://doi.org/10.1007/s40964-020-00161-3

Pang, J. S., Ansari, M. N. M., Zaroog, O. S., Ali, M. H., & Sapuan, S. M. (2014). Taguchi design optimization of machining parameters on the CNC end milling process of halloysite nanotube with aluminium reinforced epoxy matrix (HNT/Al/Ep) hybrid composite. *HBRC Journal*, *10*(2), 138–144. https://doi.org/10.1016/j.hbrcj.2013.09.007

Pasha, A., & Rajaprakash, B. M. (2022). Effect of CNT content on microstructure and hardness of AlSi/MWCNT nano composite. *Materials Today: Proceedings*, *49*, 1345-1350.

Pathak, S. R., Sharma, P., Mali, H. S., & Malik, A. (2024). Optimization of machining parameters during milling on glass fiber-reinforced textile composite. *Multiscale and Multidisciplinary Modeling, Experiments and Design*, *7*(1), 249–261. https://doi.org/10.1007/s41939-023-00204-6

Paul, S., Singh, A. K., & Ghosh, A. (2017). Grinding of Ti-6Al-4V Under Small Quantity Cooling Lubrication Environment Using Alumina and MWCNT Nanofluids. *Materials and Manufacturing Processes*, *32*(6), 608–615. https://doi.org/10.1080/10426914.2016.1257797

Pawar, S. Y., Haider, J., Pintaude, G., Sekar, S. M., Kolhe, V., Chandratre, K., Sonawane, S., & Ritapure, P. (2023). Mechanical and Tribological Behavior of LM26/SiC/Ni-Gr Hybrid Composites. *Journal of Composites Science*, *7*(4). https://doi.org/10.3390/jcs7040159

Pawar, S. Y., & Kharde, Y. R. (2020). Tribological characterization of LM26/SiC/Ni.-Gr. Hybrid aluminium matrix composites (HAMCs) for high temperature applications. *Materials Today: Proceedings*, *37*(Part 2), 793–800. https://doi.org/10.1016/j.matpr.2020.06.003

Peng, T., & Chang, I. (2014). Mechanical alloying of multi-walled carbon nanotubes reinforced aluminum composite powder. *Powder Technology*, *266*, 7–15. https://doi.org/10.1016/j.powtec.2014.05.068

Prakash, C., Selvakumar, S., Manikandan, D., & Ramaswamy, K. (2025). Machinability analysis of LM26 aluminium metal matrix composites reinforced with graphite and fly ash using the AWJM process. *Scientific Reports*, *15*(1), 1–16. https://doi.org/10.1038/s41598-025-04713-x

Prakash, C., Senthil, P., Manikandan, N., & Palanisamy, D. (2022). Investigations on machinability characteristics of Cast

Aluminum Alloy based (LM 26+Graphite+Fly ash) Hybrid Metal Matrix Composites for automobile components. *Materials and Manufacturing Processes*, *37*(7), 748–763. https://doi.org/10.1080/10426914.2021.1962531

Premnath, A. A., Alwarsamy, T., & Rajmohan, T. (2012). Experimental investigation and optimization of process parameters in milling of hybrid metal matrix composites. *Materials and Manufacturing Processes*, *27*(10), 1035–1044. https://doi.org/10.1080/10426914.2012.677911

Priya, I. I. M., Palanikumar, K., Senthilkumar, N., & Prabha, P. S. (2024). Investigation of delamination and surface roughness in end milling of glass fiber reinforced polymer composites using Fuzzy Model and Grey Wolf Optimizer. *International Journal on Interactive Design and Manufacturing*, *18*(2), 749–769. https://doi.org/10.1007/s12008-023-01576-2

Rajeswari, B., & Amirthagadeswaran, K. S. (2017). Experimental investigation of machinability characteristics and multi-response optimization of end milling in aluminum composites using RSM-based grey relational analysis. *Measurement: Journal of the International Measurement Confederation*, *105*, 78–86. https://doi.org/10.1016/j.measurement.2017.04.014

Sharif, A. (2022). Study on burr formation, tool wear and surface quality in machining Al6063. *Journal of Materials and Manufacturing*, *22*. https://doi.org/https://doi.org/10.5281/zenodo.7472023

Sharma, R., Sasikumar, C., & Baral, J. (2024). Wear behaviour of Al-MWCNT composites by varying MWCNTs concentration. *Journal of Alloys and Metallurgical Systems*, *7*, 100104. https://doi.org/10.1016/j.jalmes.2024.100104

Shihab, S. K., Gattmah, J., & Kadhim, H. M. (2021). Experimental Investigation of Surface Integrity and Multi-Objective Optimization of End Milling for Hybrid Al7075 Matrix Composites. *Silicon*, *13*(5), 1403–1419. https://doi.org/10.1007/s12633-020-00530-1

Sravanthi, K., Mahesh, V., Rao, B. N., Fernandez, G., & Haiter, L. A. (2022). Carbon-Filled E-Glass Fibre-Reinforced Epoxy Composite: Erosive Wear Properties at an Angle of Impingement. *Advances in Materials Science and Engineering*, *2022*. https://doi.org/10.1155/2022/8725305

Sreenivasulu, R. (2013). Optimization of surface roughness and delamination damage of GFRP composite material in end milling using taguchi design method and artificial neural network. *Procedia Engineering*, *64*, 785–794. https://doi.org/10.1016/j.proeng.2013.09.154

Sridhar, R., Perumal Subramaniyan, S., & Ramesh, S. (2019). Optimization of Machining and Geometrical Parameters to Reduce Vibration While Milling Metal Matrix Composite. *Transactions of the Indian Institute of Metals*, *72*(12), 3179–3189. https://doi.org/10.1007/s12666-019-01783-0

Sridhar, I., & Narayanan, K. R. (2009). Processing and characterization of MWCNT reinforced aluminum matrix composites. *Journal of Materials Science*, *44*(7), 1750-1756.

Stergioudi, F., Prospathopoulos, A., Farazas, A., Tsirogiannis, E. C., & Michailidis, N. (2022). Mechanical Properties of AA2024 Aluminum/MWCNTs Nanocomposites Produced Using Different Powder Metallurgy Methods. *Metals*, *12*(8), 1315. https://doi.org/10.3390/met12081315

Thomas, L. M., & Sreekanth, M. S. (2025). Multiwalled Carbon Nanotubes Reinforced Polyvinyl Alcohol Nanocomposites: Synergistic Enhancement on Multifunctional Performance and Deep Learning-Driven Predictions for Next-Generation Flexible Electronics. *Polymers for Advanced Technologies*, *36*(8). https://doi.org/10.1002/pat.70294

Uthale, S., Shinde, D., Shahapure, N., Kulkarni, S., & Nikam, M. (2024). Effect of MWCNTS on the mechanical properties of woven fabric hybrid polymeric nanocomposites and finite element analysis of nanocomposites. *International Journal on Interactive Design and Manufacturing*, *18*(10), 7477–7494. https://doi.org/10.1007/s12008-023-01225-8

Zeelanbasha, N., Senthil, V., Sylvester, B. S., & Balamurugan, N. (2017). Modeling and experimental investigation of LM26 pressure die cast process parameters using multi-objective genetic algorithm (MOGA). *Metalurgija*, *56*(3–4), 307–310.

© 2026 by the authors; licensee Growing Science, Canada. This is an open access article distributed under the terms and conditions of the Creative Commons Attribution (CC-BY) license (http://creativecommons.org/licenses/by/4.0/).